OPEN ACCESS

Plasma Electrolytic Oxidation Synthesis of Heterostructured TiO_2/Cu_xO Films for Photoelectrochemical Water Splitting Applications

To cite this article: R. Levinas *et al* 2024 *J. Electrochem. Soc.* **171** 036501

Journal of The Electrochemical Society, 2024 **171** 036501

Plasma Electrolytic Oxidation Synthesis of Heterostructured TiO_2/Cu_xO Films for Photoelectrochemical Water Splitting Applications

R. Levinas,[1,z] V. Pakstas,[1] A. Selskis,[1] T. Murauskas,[2] R. Viter,[3] A. Anspoks,[4] I. Pudza,[4] A. Kuzmin,[4] L. Tamasauskaite-Tamasiunaite,[1,*] H. Cesiulis,[2] and E. Norkus[1,*]

[1]*Center for Physical Sciences and Technology, Vilnius, Lithuania*
[2]*Vilnius University, Faculty of Chemistry and Geosciences, Vilnius, Lithuania*
[3]*Institute of Atomic Physics and Spectroscopy, University of Latvia, Riga, Latvia*
[4]*Institute of Solid State Physics, University of Latvia, Riga, Latvia*

TiO_2 is a versatile photo-/electrochemically active material that finds a wide variety of applications in industry and science alike. Its main but often overlooked advantage is the abundance of Ti in nature, as it is the 9th most commonly found element in the Earth's crust. Despite some drawbacks (e.g., large band gap) that limit its light conversion efficiency in comparison to some other materials, it is particularly inert in corrosive media, and its properties can be modified by various means. In this study TiO_2 films are synthesized by an anodization-like procedure called plasma electrolytic oxidation. By varying synthesis conditions different morphologies and structures are obtained. Moreover, successful heterostructuring is achieved by adding a copper precursor into the solution. The TiO_2/Cu_xO films are comprehensively characterized for their structural, optical, and photoelectrochemical properties. Interpretation of XPS and XANES spectra suggest that the content of Cu^{2+} increases in relation to the maximum voltage reached during synthesis. The UV–vis absorption was also found to display a distinct Cu^{2+} absorption footprint, as well as lower optical band gap values for the heterostructures. A comprehensive photoelectrochemical characterization for water splitting in 1 M KOH reveals that the TiO_2/Cu_xO films exhibit improved activity overall.

 [DOI: 10.1149/1945-7111/ad2ba7]

Manuscript submitted November 25, 2023; revised manuscript received January 17, 2024. Published March 4, 2024.

Supplementary material for this article is available online

In order to balance humanity's increasing need for energy and sustainability, technologies must be developed to efficiently take advantage of alternative energy sources. Sunlight, although admittedly suffering from the drawback of intermittency, can provide virtually infinite energy. In conventional photovoltaics solar energy is converted into electrical energy, which can then be stored or used to power devices. Another similar but fundamentally different course would be to convert solar energy into (electro)chemical energy, through either photocatalytic or photoelectrochemical (PEC) processes. In this case a material must be used to absorb light and produce excitons. The first discovery of PEC water splitting on TiO_2 is commonly attributed to the seminal work by *Fujishima & Honda*,[1] and it paved the way for decades of research on the photoanodic processes on TiO_2 and other transition metal oxides.

Further research on TiO_2 is crucial for addressing renewable energy issues due to its remarkable properties in photocatalysis and solar energy conversion.[2] Chief among its major drawbacks is the wide bandgap (3.0–3.2 eV),[3] limiting the absorption of longer-wavelength visible light. However, TiO_2 is abundantly found in nature, exhibits good chemical stability and is resistant to photocorrosion, making it an excellent photoanode material.[4–6] Its photocatalytic abilities enable the efficient conversion of solar energy into clean fuels like hydrogen[7,8] and the degradation of pollutants such as organics, antibiotics or pesticides,[9–11] highlighting its potential for sustainable energy production and environmental remediation.

As mentioned before, the main limiting factor of TiO_2 applications for PEC processes is its large band gap, allowing for the absorption of only ~3% of the solar spectrum.[12] Much research is being devoted to obtaining stable TiO_2-based systems with lower band gaps. For example, doping TiO_2 with transition metal ions such as Fe, Ni, or Cr introduces additional energy levels, reducing the band gap and promoting visible light absorption.[13,14] Another approach is heterostructuring TiO_2 with other semiconductors like ZnO or CuO, which alters the electronic structure and can result in narrowing the band gap.[12,15,16] Copper oxide in particular may be interesting for PEC applications, because it has a low band gap of ~1.7 eV[17] and unique selectivity for methanol oxidation[18]—a prospective characteristic in fuel cell applications. Surface modifications, such as depositing noble metal nanoparticles or carbon-based materials, can create localized energy states, effectively lowering the band gap of TiO_2 photoanodes and improving PEC performance.[19–21]

Many methods exist to synthesize TiO_2 films for PEC applications, the more common among them being sol-gel synthesis,[22] chemical vapor deposition,[23] and electrochemical synthesis. For the latter, TiO_2 can be obtained either by cathodic deposition from a precursor solution[24] or, more commonly, anodization.[25–27] Anodization is particularly versatile as it can yield films of various nanostructured morphologies, but most often an amorphous material is obtained,[28] which is then annealed to obtain an anatase crystalline structure that is desirable for PEC applications.

Combining electrochemical synthesis of TiO_2 with heterostructuring can be easily achieved using a method called plasma electrolytic oxidation (PEO), sometimes referred to as microarc oxidation (MAO). The initial steps of this synthesis are identical to anodization, but at larger voltages localized micro-sized plasma discharges and dielectric breakdown begin to occur,[29] which typically yields the anatase TiO_2 phase.[30] The plasma can ionize any electrolyte in contact with it and create a mixture, which then cools and solidifies, resulting in a composition that includes ions from the solution. This phenomenon is already widely used in synthesizing biomedical TiO_2-based implants with, for example, Ca for improved biocompatibility.[31] However, as shown previously by our group, there exists enormous potential to use PEO for synthesis of transition-metal-oxide based heterostructured materials for PEC applications.[32]

Therefore, the aim of this study was to synthesize TiO_2/Cu_xO heterostructures by PEO and characterize their PEC performance as photoanodes. To do this, the synthesis conditions (electrolyte, voltage, temperature) had to be carefully controlled in order to

*Electrochemical Society Member.
[z]E-mail: ramunas.levinas@ftmc.lt

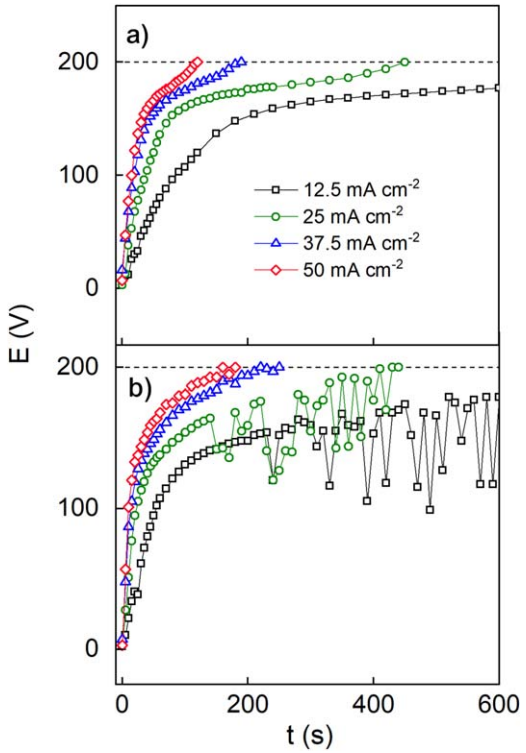

Figure 1. Cell potential-time responses for Ti plasma electrolytic oxidation at different applied current densities in (a) 0.1 M NaOH +0.05 NaH_2PO_2; (b) 0.1 M NaOH +0.05 M NaH_2PO_2 + 0.1 M $CuSO_4$ + 0.1 M Na_3cit.

reach appropriate and reproducible results. The morphology and structure of the synthesized films were comprehensively investigated and related to synthesis conditions. The films were used as photoanodes for anodic water splitting in 1 M KOH, additionally evaluating the influence of a hole scavenger—methanol.

Experimental

Plasma electrolytic oxidation.—PEO was carried out in a two-electrode cell with a stainless-steel cathode, and the working electrode as the anode. The working electrode was Ti foil (0.25 mm, 99.5%, Alfa Aesar) of 1 × 1 cm dimensions and a total 2 cm^2 working area. Before synthesis, the Ti foil was etched for 1 min in a 1:1 solution of concentrated HF and water to make the surface rougher. During PEO the solution was stirred magnetically. In order to control the solution temperature, the cell was kept in a water bath to better dissipate the produced heat. It was observed that over a typical synthesis the solution temperature could increase by 1 to 2 °C. All syntheses were started at 20 °C. A high-voltage power source (Consort EV245) and different applied currents (25, 50, 75, and 100 mA) were used for characterization of the process. The base electrolyte to dissolve Ti and produce TiO_2 was 0.1 M NaOH (⩾99%, Roth). To enable PEO, 0.05 M NaH_2PO_2 (⩾99%, Roth) was added. Furthermore, to deposit the TiO_2/Cu_xO heterostructure, 0.1 M $CuSO_4$•$5H_2O$ (⩾99.5%, Roth) and 0.1 M tri-sodium citrate dihydrate (⩾99%, Roth) were added. An insoluble $Cu(OH)_2$ precipitate forms in alkaline media, so Na_3cit was necessary to dissolve $CuSO_4$, as it forms soluble complex compounds with Cu^{2+} ions. The synthesized films were dried and kept in air until further experiments.

Structural characterization.—The surface morphology was observed by a SU-70 FE-SEM. Focused ion beam (FIB) cross-sectional analysis was carried out using a FEI Helios Nanolab 650 dual beam system.

XRD patterns of the TiO_2 and TiO_2/Cu_xO thin films were measured using an X-ray diffractometer SmartLab (Rigaku) equipped with 9 kW rotating Cu anode X-ray tube. Grazing incidence (GIXRD) method was used in 2θ range 15°–80°. An angle between parallel beam of X-rays and a specimen surface (ω angle) was adjusted to 0.5° degrees. Phase identification was performed using software package PDXL (Rigaku) and ICDD powder diffraction data-base PDF-4+ (2022 release). The approximate size of the synthesized TiO_2/Cu_xO heterostructures was calculated based on the broadening of XRD peaks using the graphical Halder–Wagner method implemented into PDXL software.

The XPS analyses were carried out with a Kratos Axis Supra spectrometer, using a monochromatic Al K(alpha) source (25 mA, 15 kV). Survey scan analyses were carried out on the area of 300 × 700 μm at a pass energy of 160 eV. High-resolution analyses were carried out also on the area of 300 × 700 μm, but at a pass energy of 20 eV. The XPS signal due to adventitious carbon located at 284.8 eV was used as a binding energy (BE) reference.

X-ray absorption spectroscopy.—X-ray absorption experiments were performed at the DESY PETRA-III P65 beamline.[33] The storage ring operated at $E = 6.08$ GeV and $I = 120$ mA in a top-up 480 bunch mode. The fixed-exit double-crystal monochromator Si (111) was used to scan the required energy range, and harmonic reduction was achieved by the use of two Rh-coated silicon plane mirrors. The X-ray absorption spectra were collected at the Cu K-edge (8979 eV) in fluorescence mode at room temperature using a passivated implanted planar silicon (PIPS) detector (Canberra). Copper foil and polycrystalline CuO powder were used as reference compounds and were measured in transmission mode using two ionization chambers. X-ray absorption near-edge structure (XANES) and extended X-ray absorption fine structure (EXAFS) spectra were extracted and analyzed using the XAESA code[34] following a conventional procedure.[35]

Optical properties and FTIR.—Diffuse reflectance spectra were measured in the range of 250–900 nm by means of Ocean Optics HR4000 spectrometer (Ocean Insight, Orlando, FL, USA), Ocean Optics reflectance probe (angle 45°) and deuterium-halogen light source (DH-2000-BAL). Diffuse reflectance R was converted to absorbance F using known Kubelka-Munk equation:

$$F = \frac{(1-R)^2}{2 \cdot R} \quad [1]$$

The band gap E_g was graphically calculated from the equation:

$$(F \cdot h\nu)^{1/2} = A(h\nu - E_g) \quad [2]$$

FTIR spectra have been measured by ATR mode using Bruker Alfa II spectrometer (Karlsruhe, Germany). The samples were tightly pressed to the FTIR crystal. Measurements have been performed in absorption mode in the range of 3500–400 cm^{-1} with 2 cm^{-1} resolution.

Photo/electrochemical characterization.—The PEC properties of the films were investigated in a quartz glass three electrode cell, with an Ag/AgCl reference electrode and a stainless-steel counter electrode. The potentials presented in the study have been recalculated vs RHE. For general characterization a 1 M KOH (⩾85%, Roth) electrolyte was used. Up to 5% of methanol was added to the 1 M KOH solution to investigate the effect of a hole scavenger. All PEC experiments were carried out with an Autolab 302 N potentiostat, connected to an Autolab LED driver and optical bench system. The light source was a 365 nm Thorlabs LED calibrated to a light intensity of 25 mW cm^{-2}. A typical characterization consisted of a chopped-light linear sweep voltammetry (LSV) scan from 0.4 V to 2.2 V at 5 mV s^{-1}, and a subsequent potentiostatic pulse at 1.23 V. Where needed, the photocurrent was calculated by subtracting the background current from the photocurrent at the end of the pulse ($j_{ph} = j_{t\ =\ 30} - j_{bg}$). The behavior of the photocurrent over 2 h was investigated potentiostatically at 1.23 V, by illuminating the

photoanode with 2 s "light off" pauses every 10 min. Incident photon conversion efficiencies (IPCE) were calculated by Eq. 3.

$$IPCE(\%) = \frac{j_{ph}\,(\mathrm{mAcm^{-2}}) \times 1240\ \ (V\mathrm{nm})}{I_0\ \ \ (m\mathrm{Wcm^{-2}})\ \ \ \times \lambda\ \ (\mathrm{nm})} \qquad [3]$$

The Mott-Schottky analysis was performed by measuring the electrochemical impedance of the films at potentials from 1.2 V to −1 V (vs Ag/AgCl) at 50 mV increments. Instead of a full spectrum, 4 points (1000 Hz, 700 Hz, 400 Hz, 100 Hz) were measured. These points were then fitted to a typical Randles circuit, and the calculated capacitance was used to draw the Mott-Schottky plots.

Intensity modulated photocurrent spectroscopy (IMPS) experiments were carried out at potentials from 0.4 V to 1.8 V in 1 M KOH without and with 5% CH_3OH. The light intensity (25 mW cm^{-2}) was subjected to 10% modulation by amplitude.

Results and Discussion

Obtaining of photoanodes.—For process characterization synthesis was carried out until a voltage maximum of 200 V. Initially, TiO_2 films were synthesized in 0.1 M NaOH without any additives (Fig. S1). Regardless of applied current, the voltage maximum was never reached, and a plateau of ∼170 V was only obtained with 50 mA cm^{-2}. Rapid and strong breakdowns of the oxide layer were observed, particularly after some time at the lower current densities, which manifest as a sharp drop in voltage. When 0.05 M NaH_2PO_2 is added to the solution, the voltage behavior over time at constant current becomes more typical of a PEO process (Fig. 1a). The general mechanism of PEO on Ti is comprised from three stages,[36] which can be distinguished in this synthesis as well. Stage I is where a linear relation exists between E – t as the oxide film grows mainly due to the typical anodization mechanism. The slope of E – t depends of the applied current and ranges from 0.73 V s^{-1} at 12.5 mA cm^{-2} to 4.9 V s^{-1} at 50 mA cm^{-2}. The end of Stage I is E_b – the breakdown voltage – where micro-sized sparks caused by ionization of the film and electrolyte appear on the surface. This means that the total current is now a sum of the electric current and a new ionic current component, so the E – t slope begins to plateau. This is called Stage II and is characterized by the occurrence of plasma sparks/emissions and a lower E—t slope. Eventually the voltage reaches a critical value (E_c), and after this stage III begins. A sharper E—t curve turn is observed again, which is caused by vigorous PEO, sparks appearing on the surface, and a dominating ionic current component. In this case stage III was not carried out until completion (the final voltage V_f), because a maximum of 200 V was set.

When synthesizing the TiO_2/Cu_xO heterostructures the same tendencies can be observed, but the oxide is more prone to breakdowns, as can be inferred from the choppy E—t curves (Fig. 1b). It is likely that this is caused by the incorporation of CuO into the TiO_2 film, and therefore weaker dielectric properties of the film. The three PEO stages are also less pronounced, but for stage I, an E—t slope of 1.62 V s^{-1} to 5.65 V s^{-1} (from 12.5 mA cm^{-2} to 50 mA cm^{-2} respectively) can be calculated, both slightly larger than for TiO_2.

In preliminary experiments it was determined that the best PEC properties can be obtained when the films had been synthesized at 50 mA cm^{-2}. These conditions also require the shortest synthesis time. Because the films were primarily synthesized to act as photoanodes, all further characterization has been performed on films that had been obtained at 50 mA cm^{-2}.

For morphological, structural, and optical characterization three synthesis conditions were chosen by maximum synthesis voltage (E_{max})—120, 160, and 200 V for both TiO_2 and TiO_2/Cu_xO. Initially, the surface morphology of the synthesized films was observed by SEM. For plain TiO_2 (Figs. 2a–2c) at 120 V (Fig. 2a) the morphology is compact and features scattered pores and discharge channels left after cooling of ejected plasma. At 160 V (Fig. 2b) a more "PEO-like" structure is formed, consisting of disordered sub-micrometer sized cavities/pores and a smooth albeit uneven surface. When the film had been synthesized up to 200 V (Fig. 2c) the overall structure is thicker and pores are wider. The surface morphology of the TiO_2/Cu_xO films (Figs. 2d–2f) follows the same trend with E_{max}, but the film synthesized up to 120 V (Fig. 2d) already shows a fairly evolved and porous structure. Consequently, at 160 V (Fig. 2e) the TiO_2/Cu_xO film already has large pores and a thick interpore layer, while at 200 V (Fig. 2f) the edges of the pores appear cracked, probably due to powerful plasma eruptions. The thicknesses of these films were approximated from FIB cross-sections, which are shown in the insets for their respective films in Fig. 2. For plain TiO_2 films synthesized to 120 V, 160 V and 200 V they are 240 nm (±16 nm), 380 nm (±69 nm) and 850 nm (±315 nm). The comparable heterostructured films were thicker: 311 nm (±26 nm), 543 nm (±148 nm), 1307 nm (±253 nm). It is also apparent that film thickness is not uniform, and the deviation

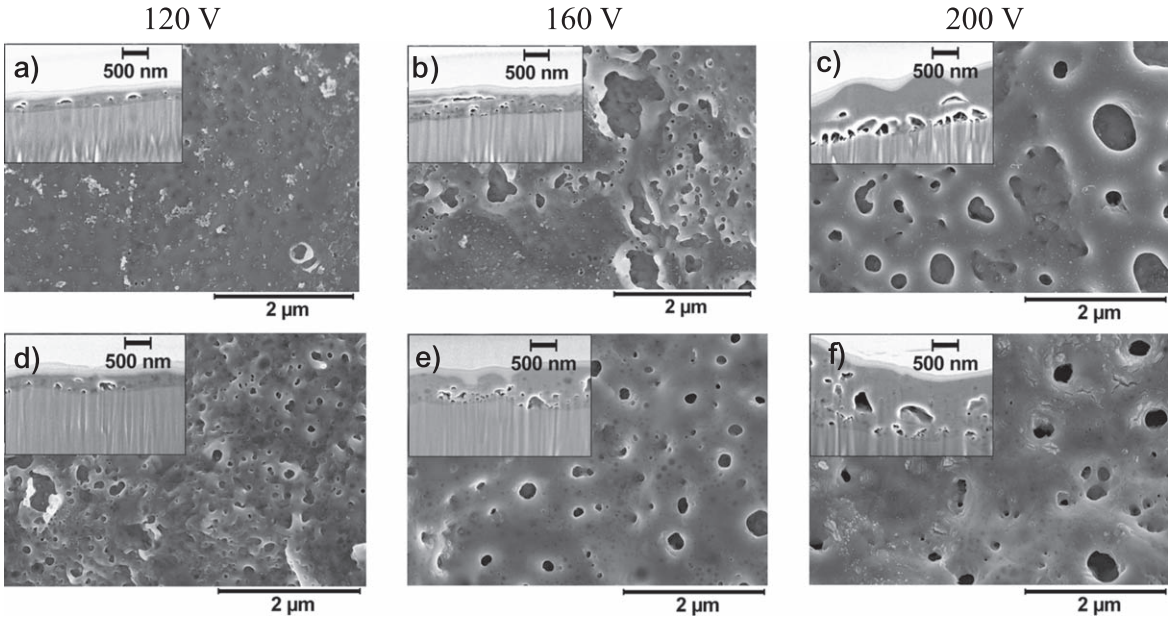

Figure 2. SEM surface morphology and FIB cross-sections (in insets) of (a), (b), (c) TiO_2 and (d), (e), (f) TiO_2/Cu_xO films.

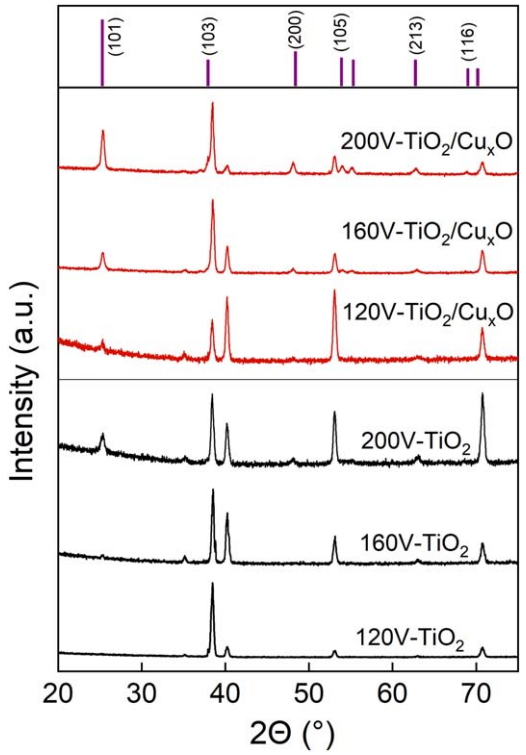

Figure 3. Grazing angle X-ray diffractograms of TiO_2 and TiO_2/Cu_xO films, synthesized to different voltage caps. Reference ICDD card of anatase 00-064-0863.

between the thinnest and thickest points are larger for the thicker films. It is worth noting that, although the film thickness appears to be exponentially proportional to voltage (Fig. S2a), it is in fact linearly related to synthesis time (Fig. S2b).

XRD measurements were used to characterize the crystalline structure of the synthesized films. The diffractograms were obtained in grazing incidence mode, but a strong hexagonal crystal structure Ti substrate (ICDD # 00-044-1294) signal could still be seen at $2\Theta = 35.09$; 38.42; 40.17; 53.01 and 62.95° (Fig. 3). The peaks emerging at $2\Theta = 25.31$, 37.00, 48.03, 53.98, 55.06 and 68.88 with increasing E_{max} are attributed to the crystallographic planes (101), (103), (200), (105), (211) and (116) respectively, of the tetragonal structure of anatase (ICDD # 00-064-0863).[37,38] It is evident that the films exhibit improved crystallinity as E_{max} is increased from 120 V to 200 V. However, there is also a difference between the plain and heterostructured films. For TiO_2 a discernible (101) peak is only displayed by the 200V-TiO_2 sample. In contrast, the diffractograms of all TiO_2/Cu_xO films have the (101) and (200) peaks, with the 200V-TiO_2/Cu_xO sample having the most intense anatase TiO_2 peaks overall. An increase in the intensity of these diffraction peaks can be attributed to the increasing thickness of the films. The difference in the crystallinity of the TiO_2 and TiO_2/Cu_xO films may be related to the presence of citrate in the PEO solution for heterostructures. TiO_2 crystallite sizes increased from 5–8 nm for samples without Cu_xO to 16.6–21.8 nm for TiO_2/Cu_xO. It had been shown that different organic additives can change the PEO mechanism and kinetics,[39] and consequently the properties of the films. No copper or other TiO_2 phases (e.g., rutile) were observed by XRD. In order to have more quantitative information, the elemental composition of the heterostructured films was measured by EDX, and the results are presented in Table S1. All ions from the solution —Cu, S, P, and Na—are detected in the films, and their quantities vary with the maximum synthesis voltage. The largest amounts of Cu, P, and Na are found in the 200V-TiO_2/Cu_xO film. These elements incorporate into the film when the ionized TiO_2 plasma comes in contact with the electrolyte and then solidifies again.

XPS was used to more accurately study the presence of Cu in the heterostructured films. All oxidation states—Cu, Cu^+ and Cu^{+2}—were detected in varying quantities based on E_{max}. The spectra of all samples show a Cu signal, comprised from the main photoemission peaks of $Cu2p_{3/2}$ at 933 eV and $Cu2p_{1/2}$ at 952 eV (Fig. S3). This spin–orbit separation of 19 eV is in good agreement with values presented in literature.[40] Satellite shake-up structures that are indicative of the presence of CuO[41] were also observed at binding energies ∼10 eV higher than the respective Cu2p main peaks. The $Cu2p_{3/2}$ peak with its adjacent shake-up satellites was further deconvoluted to evaluate the oxidation state of surface Cu on the synthesized heterostructured films (Fig. 4). Here the Cu° binding energy was ∼932.3 eV. The signal with the nearest binding energy was attributed to Cu_2O (∼931.7 eV), and CuO was distinguished by its slightly larger binding energy as well as shake-up structures.[42] First of all, it is apparent that for the 120V-TiO_2/Cu_xO film the $Cu2p_{3/2}$ peak is dominated by the Cu° signal (Fig. 4a). In contrast, the films that had formed after reaching higher E_{max} have a stronger CuO signal and more pronounced shake-up satellites (Figs. 4b, 4c). For 160V-TiO_2/Cu_xO in particular the $Cu2p_{3/2}$ peak splits into two components, one of which is attributed to CuO (934.5 eV).

The O1s spectra are also interesting in that three peaks are distinguished for all films. The Ti2p spectra showed ∼100% Ti^{+4}, so only one oxidation state for O is expected with regard to Ti. The O 1s peak at 530 eV is typically related to the Ti-O bonds in TiO_2, and the peak at slightly larger binding energies (531–532 eV) to Ti-OH.[43,44] Similarly, the Cu-O bonds in CuO are expected to display a main O 1 s peak at ∼529.8 eV, and a Cu-OH side peak at 531.2 eV.[45] It is then impossible to distinguish Ti and Cu oxides from the O 1 s peak alone, but it is also evident that when PEO occurs to a higher voltage, more Ti/Cu hydroxides form on the surface.

Moreover, the Cu LMM spectra can be used to better distinguish between the existing Cu oxidation states. Peaks at ∼918.8 eV and ∼917.9 eV can be attributed to Cu° and Cu^{+2}, whereas Cu^+ should give a peak signal at ∼916.9 eV.[46] From the spectra in Fig. 5 a certain tendency can be seen: as the E_{max} increases from 120 V to 200 V, the broad peak at 918 eV which is probably comprised from the Cu and CuO signals decreases. Consequently, the peak at 917 eV grows, meaning a stronger Cu_2O signal. This suggests that the 120V-TiO_2/Cu_xO film has a relatively large amount of Cu (which agrees well with its respective $Cu2p_{3/2}$ spectrum). The sample that had been synthesized up to the highest voltage shows a much stronger Cu_2O signal, and the 160V-TiO_2/Cu_xO represents an intermediate case with weak but distinct signals of all three copper oxidation states. It is also evident that the 200V-TiO_2/Cu_xO film has a broad peak at ∼915 eV. According to literature,[47] such Auger peak kinetic energies may correspond to certain copper halogenides, sulfides, or phosphates ($Cu_3(PO_4)_2$ $E_k = 915.76$ eV). Then the appearance of this peak could perhaps be related to the larger amount of P measured in the composition of these films with increasing synthesis voltage (Table S1). Additionally, the peak/band at ∼921 eV could be attributed to the Na KLL Auger signal,[48] which appears because of Na incorporation into the film during PEO.

XANES.—Comparing X-ray absorption near edge spectra (shown in Fig. 6) of the 200V-TiO_2/Cu_xO sample with CuO (Cu^{+2}) and Cu foil (Cu°), we can see that it is very close to CuO. Pre-edge features around 8984 eV seen as a shoulder and the position of the main peak at 8987 eV strictly coincide with the corresponding features of CuO. Also, the following trend of the spectra is very close, and existing differences are mainly due to nanosized and off-stoichiometry effects. Presence of metallic Cu should result in a pre-edge feature around 8980 eV, which is very pronounced as seen in Cu foil spectrum and weakly depends on structure. Also rest of the spectrum significantly differs from the metallic Cu. Regarding the presence of Cu^+, a mixture of CuO and Cu_2O can be expected to give a spectrum visually similar to CuO, but the main peak should shift toward lower energy values.[49,50]

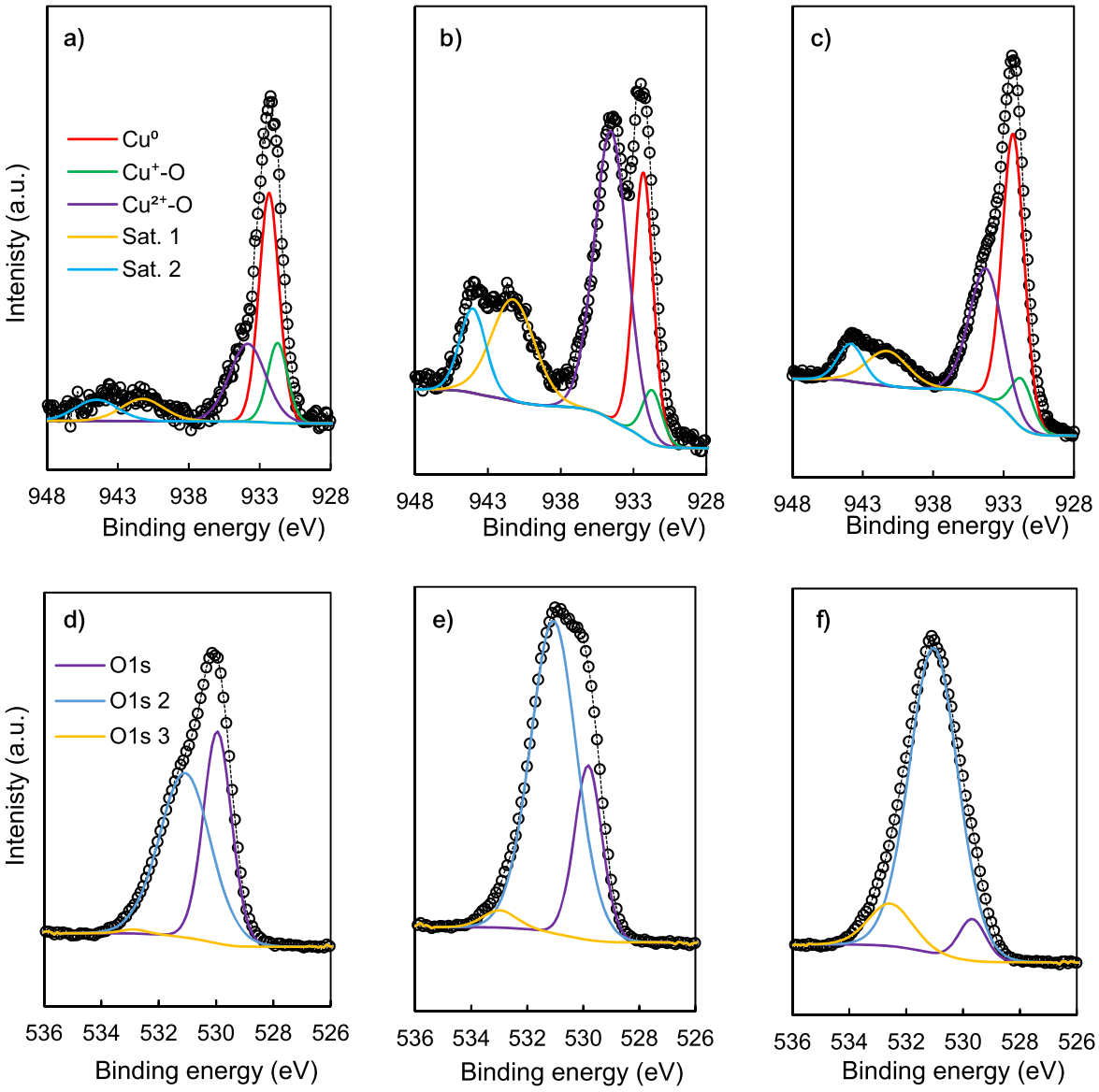

Figure 4. Cu2p$_{3/2}$ and O1s core-level and deconvoluted peaks for (a), (d) 120V-TiO_2/Cu_xO, (b), (e) 160V-TiO_2/Cu_xO, (c), (f) 200V-TiO_2/Cu_xO.

Comparing the spectra of 200V-TiO_2 and CuO, this clearly does not happen. Therefore, the dominant oxidation state is Cu^{+2}.

Comparing EXAFS of the 200V-TiO_2/Cu_xO sample with CuO and Cu we can also confirm that it is very close to CuO (Fig. S4a). As the spectrum is very noisy, it is better seen in the Fourier transform (FT-EXAFS) shown in Fig. S4b, where the first peak corresponds to the Cu-O distance (with maximum around 1.45 Å) and there are no additional features corresponding to Cu-Cu distance for metallic Cu (with maximum around 2.24 Å). Therefore, there is a discrepancy with XPS results, which show an appreciable Cu^0 amount in this sample. It is probable that there is a disproportionately larger amount of Cu^0 on the film's surface, potentially due to the interaction of oxidized copper with the reducing $H_2PO_2^-$ ions from the solution.

Optical properties.—The optical properties of the TiO_2 and TiO_2/Cu_xO films were characterized by diffuse UV–vis spectroscopy and FTIR. The reflectance spectra of the films that had been synthesized to 120 V overlap for TiO_2 and TiO_2/Cu_xO (Fig. S5a), which is expected owing to the similar electrochemical behavior during synthesis (the bulk of the film is formed during stage I of PEO). A more noticeable difference is seen for the 160 V (Fig. S5b) and 200 V (Fig. 7) films. Both materials have an absorption maximum in the near-UV range as expected, but a noticeable red shift towards longer wavelengths is seen for the heterostructures followed by diminished visible light absorption. The optical band gaps were graphically estimated from the intercept of the linear region of absorption with the baseline.[51] TiO_2/Cu_xO was found to have a slightly lower band gap—3.25 eV (in contrast to 3.3 eV for TiO_2, Fig. 8). The band gaps of all films fell within the 3.25 eV–3.35 eV range (Figs. S5c, S5d). Similar optical band gap values have been reported for TiO_2/CuO heterostructures.[16] It is likely that the observed red shift of the absorption maximum was caused by heterostructuring TiO_2 with a mixture of CuO and Cu_2O, which are lower band gap semiconductors. According to literature, Cu^{2+} exhibits an absorption hump up to 900 nm due to the transition of the single electron in the $3d^9$ configuration,[52] which is not observed for Cu^+ due to its $3d^{10}$ configuration. Then the rise in reflectance for TiO_2/Cu_xO with increasing E_{max} can likely be related to the increasing amount of Cu^{2+} within their structure.

The FTIR spectra of 200V-TiO_2 and 200V-TiO_2/Cu_xO heterostructures are shown in Fig. 9. Both spectra showed absorptions bands at 1055, 768, 655 and 420 cm^{-1}. Two new absorption bands had appeared at 580, 490 cm^{-1} for TiO_2/Cu_xO. It was reported that

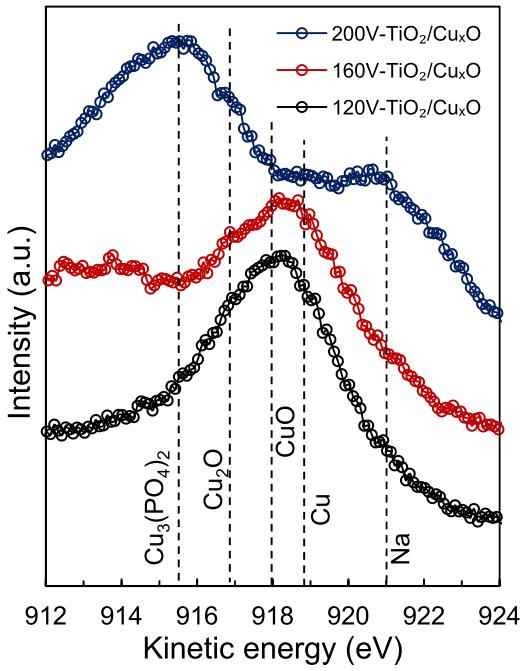

Figure 5. Stacked Cu LMM Auger plots of heterostructured films.

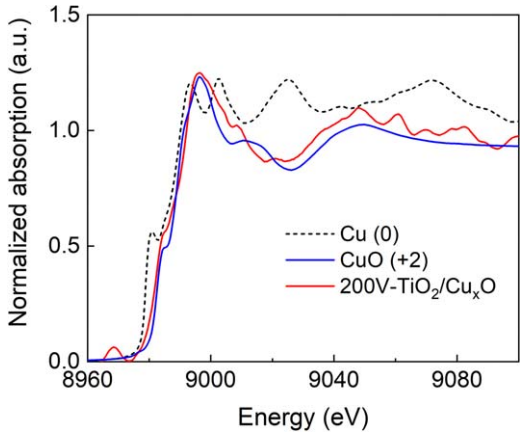

Figure 6. Cu K-edge XANES spectra of the 200V-TiO_2/Cu_xO sample compared to CuO (+2) and Cu foil (0).

Cu-O stretching vibrations are located at 518–570 cm^{-1} [53]; 432.3 cm^{-1}, 497 cm^{-1}, and 603.3 cm^{-1} (CuO phase) and 605–660 cm^{-1} (Cu_2O phase)[54]; 516 cm^{-1} [55]; 454.5 cm^{-1} and 605.7 cm^{-1}.[56] Ti-O and O-Ti-O vibrations that are located at 451, 602 and 721 cm^{-1} display the Ti-O and O-Ti-O bonding.[53,55–57] Meanwhile, Cu-Ti vibrations are located at 540 cm^{-1}.[57] The peak at 1055 cm^{-1} is related to OH vibrations.[55,56] On the basis of the reported results, we can assume that the peaks at 768, 655 and 420 cm^{-1} correspond to Ti-O and O-Ti-O vibrations, and the peaks at 580, 490 cm^{-1} correspond to Cu-O vibrations.

Photoelectrochemical characterization.—The films synthesized in this study were characterized for their PEC as photoanodes in alkaline media. A typical experimental procedure consisted of an anodic LSV scan with pulsed light, followed by a potentiostatic pulse at 1.23 V vs RHE. Representative results of such an analysis are presented in Fig. 10a. For both plain TiO_2 and the heterostructured film, photocurrent steadily grows with increasing applied potential. However, the TiO_2/Cu_xO film generates a larger photocurrent across the entire measured potential range. The background "dark" current is negligible until the applied potential approaches

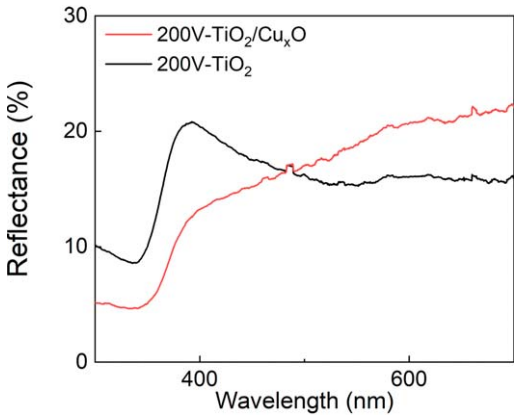

Figure 7. UV–vis reflectance spectra of 200V-TiO_2 and 200V-TiO_2/Cu_xO heterostructures.

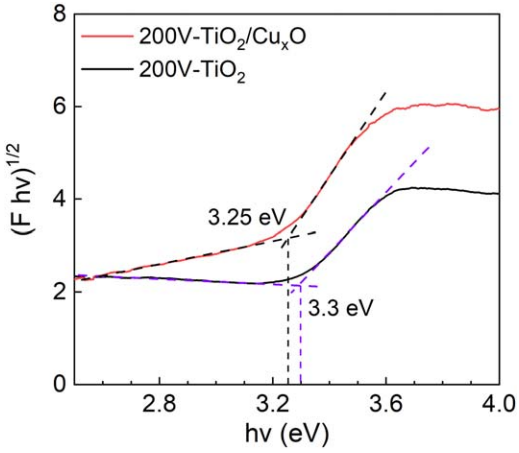

Figure 8. Tauc plots with band gap calculations of 200V-TiO_2 and 200V-TiO_2/Cu_xO heterostructures.

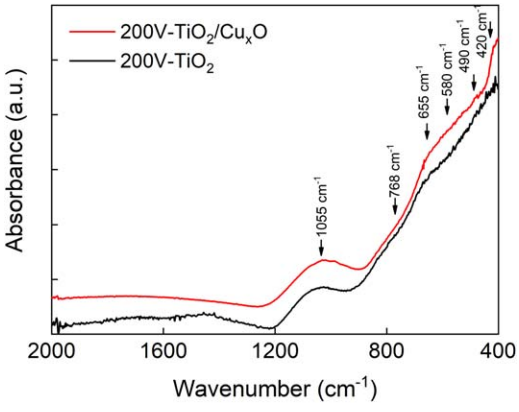

Figure 9. FTIR spectra for 200V-TiO_2 and 200V-TiO_2/Cu_xO films.

~1.8 V, where electrochemical oxygen evolution likely begins to occur. Figure 10b shows the potentiostatic light pulses measured at 1.23 V, which reproduce the LSV results but at steady-state conditions. The heterostructure generates a larger photocurrent and exhibits faster photogenerated charge carrier kinetics, as the maximum photocurrent is reached almost instantaneously with illumination. In contrast, for the plain TiO_2 film the photocurrent reaches its steady-state value after ~2 s, signaling slower photoexcited charge transfer. However, in both cases the effect is fairly weak and both pulses exhibit good stability and almost no electron-hole recombination.

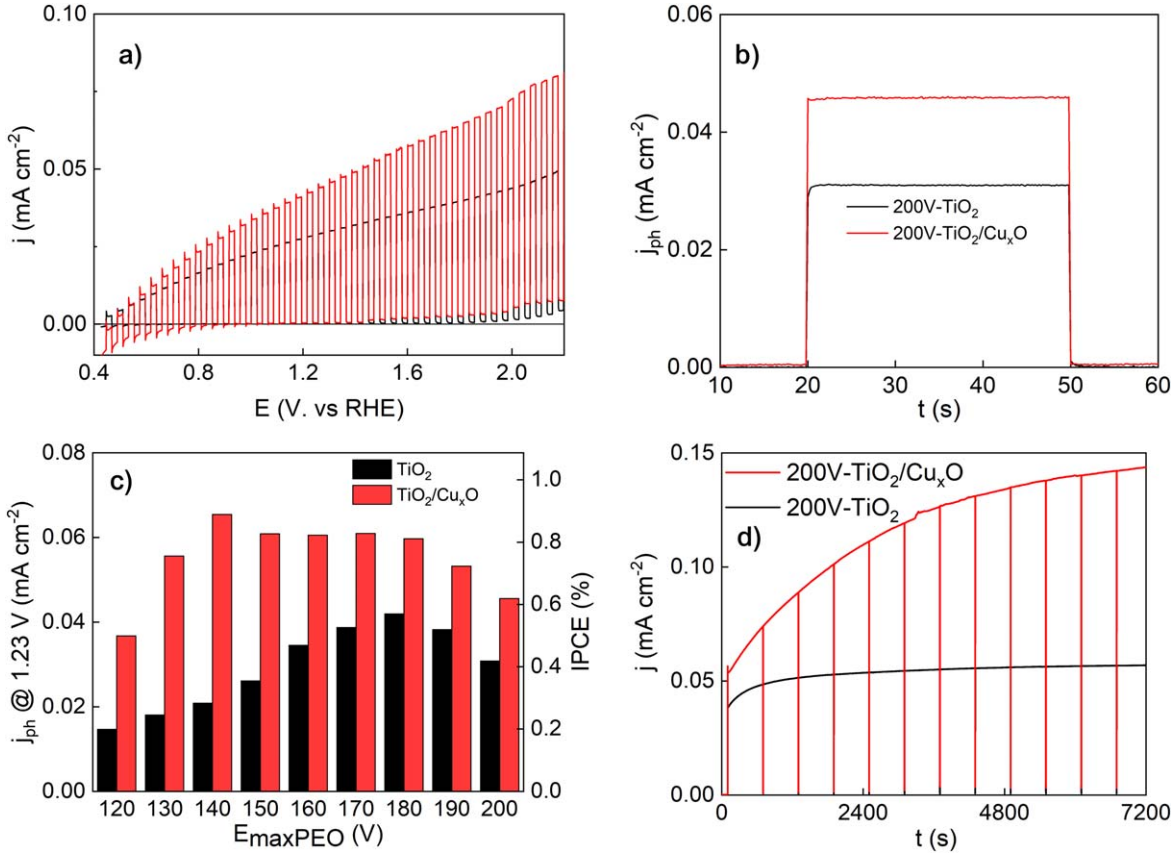

Figure 10. Photoelectrochemical properties of TiO_2 and TiO_2/Cu_xO films: (a) LSV scans at 5 mV s^{-1} with chopped illumination; (b) steady-state photocurrent pulses at 1.23 V; (c) photocurrents obtained at 1.23 V for films that had been synthesized to different E_{maxPEO} values; (d) longer-duration photoelectrochemical stability measurements.

This characterization was carried out for each synthesized film. The photocurrents obtained from the potentiostatic pulses and their respective calculated IPCE values are summarized in Fig. 10c. This figure provides an overall generalization of the PEC properties of the TiO_2 and TiO_2/Cu_xO films, and the data confirms that the heterostructures generate larger photocurrents than the comparable plain films. It is also revealed that there are certain optimal conditions that result in the best PEC activity. For plain TiO_2 films the j_{ph} generated at 1.23 V increases until a maximum is reached when the film had been synthesized to 180 V (j_{ph} = 42 μA cm^{-2}), after which a negative trend is seen. The photocurrents of the heterostructures plateau from 150 V to 180 V and generate ~60 μA cm^{-2}, with the exception of the film that had been synthesized to 140 V, which may be an outlying data point. Finally, the films were characterized for longer-duration stability by keeping constant 25 mW cm^{-2} illumination at 1.23 V for 2 h, with light off pulses every 600 s to track the background current (Fig. 10d). Over the course of this experiment both films gained photoelectrochemical activity, particularly the heterostructured sample. The increased currents are attributed to the photoelectrochemical process because the dark current does not change. This is an interesting phenomenon and has been observed for H^+-intercalated WO_3 films in our previous research,[58] where it was attributed to vacancy/defect restructuring.

Mott-Schottky and Gartner-Butler analyses.—Because it was expected that the nature of the defects in these semiconductor films could vary due to either changes in the synthesis conditions or by heterostructuring with Cu_xO, the Mott-Schottky analysis was carried out to evaluate the semiconductor properties. The Mott-Schottky equation relates the capacitance of the space-charge layer of a semiconductor with the applied potential (Eq. 4), and the flat band potential (V_{fb}) can be obtained where the $1/C_{SC}^2$-E plot intercepts the Y axis.

$$\frac{1}{C_{SC}^2} = \left(\frac{2}{q\varepsilon_r\varepsilon_0 N_D}\right)\left((E - E_{FB}) - \frac{kT}{q}\right) \quad [4]$$

Here C_{SC} is the capacitance of the space charge layer, q is the elementary charge of an electron, ε_r is the relative permittivity/dielectric constant and ε_0 is vacuum permittivity, N_D is the concentration of donors, E—the applied potential, E_{FB} the flat band potential, k is Boltzmann's constant, and T is the absolute temperature.

The results of the MS analysis presented in Fig. 11a show that the heterostructured 200V-TiO_2/Cu_xO film has a significantly larger flat band potential (V_{fb} = ~0.72 V) than the comparable 200V-TiO_2 film (V_{fb} = 0.27 V). The Mott-Schottky plots for the remaining films are shown in Fig. S6, and clearly confirm the tendency for the TiO_2/Cu_xO films to have more positive V_{fb}. For the heterostructured films V_{fb} increases with synthesis voltage, possibly due to the larger amount of Cu_xO in their composition. However, it must be kept in mind that nanostructured morphological effects may also shift V_{fb} values.[59]

Theoretically, V_{fb} should be close to the onset potential of photocurrent. To check the validity of these results, an additional method of approximating the flat band potential was employed—the Gartner-Butler analysis, as described by A. Hankin et al.[60] In this method j_{ph}^2 is plotted against overpotential, and V_{fb} is predicted to be at the intercept with the overpotential axis. The photocurrents were calculated from potentiostatic pulses like those shown in Fig. 10b. This time different V_{fb} values are obtained (0.54 V and 0.65 V for the TiO_2 and TiO_2/Cu_xO respectively) (Fig. 11b). For TiO_2/Cu_xO the V_{fb} values obtained by both methods are relatively similar, and reproducibly more positive than for TiO_2 (admittedly,

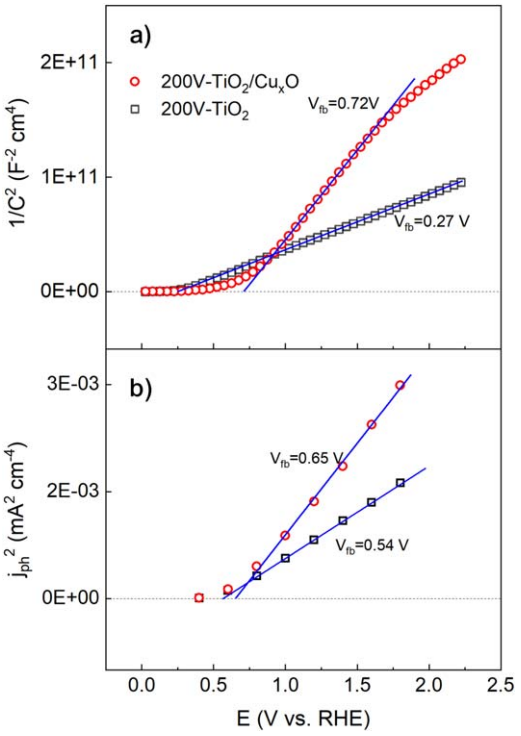

Figure 11. Flat band calculations: (a) Mott-Schottky plots; (b) Gartner-Butler plots.

the errors can be relatively large due to the approximation of the linear region). However, both methods give different values of V_{fb} for TiO_2.

This can perhaps be further analyzed by considering the photoelectrochemical properties of the respective films. As shown in Fig. S7 (which is a zoomed in version of the low overpotential region of Fig. 10a) the photocurrent onset potential is well below 0.4 V for both films. However, the electrochemical current begins at cathodic values, and approaches zero at ∼0.6 V for TiO_2 and at ∼0.75 V for TiO_2/Cu_xO. An entire n-type photocurrent pulse can even be registered at otherwise cathodic currents (Fig. S8). Then all the results from the MS, Gartner-Butler, and PEC analysis can be related and the shift in band bending confidently attributed to changes in the material's semiconductor properties by heterostructuring with Cu_xO, which shifts the flat band potential towards more positive values. Moreover, this shift can be directly related to the film synthesis voltage (which corresponds to increasing Cu_xO content) as shown in Fig. S9a. For plain TiO_2, regardless of synthesis voltage, the same effect is not seen (Fig. S9b).

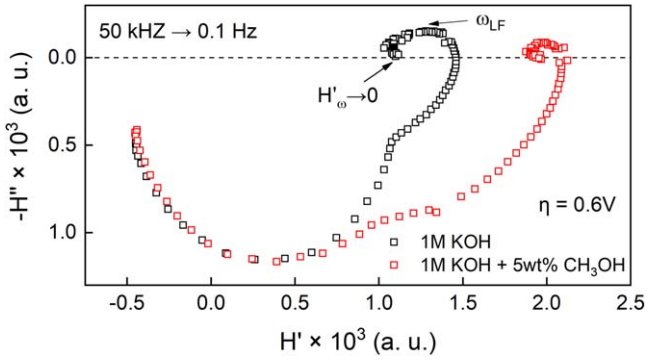

Figure 12. IMPS spectra obtained at 0.6 V for a 200V-TiO_2/Cu_xO film in 1 M KOH without and with 5% CH_3OH.

Photoelectrochemical methanol oxidation and IMPS.—As mentioned before, some of the films, particularly the TiO_2/Cu_xO heterostructures, exhibit a small but appreciable amount of surface electron-hole recombination. Oxygen evolution is a thermodynamically difficult process (E = 1.23 V), so a common strategy used to harvest more incident light is the introduction of a "hole scavenger" into the system. I. e., a material that can be oxidized at lower energies and thus "accept" the photogenerated holes from the photoanode. In this case CH_3OH was chosen as the hole scavenger. It has a lower oxidation potential and is commonly used in photoelectrochemical systems.[61,62] The same broad characterization as previously was carried out and it was observed that the photocurrent increases with methanol content (Fig. S10), so subsequent characterizations were carried out in 1 M KOH solutions with 5% CH_3OH. It was observed that CH_3OH does indeed act as a hole scavenger and improves the overall photoelectrochemical activity of the films, which manifests as a larger measured photocurrent at all overpotentials (Fig. S11).

A more advanced photoelectrochemical technique called intensity modulated photocurrent spectroscopy (IMPS) was used to establish a deeper understanding of the charge carrier photogeneration and transfer/recombination kinetics at the catalyst-solution interface. With this method the potential is kept constant, but a modulation is applied on the light intensity. The resulting response is caused by the generation and transfer/recombination of charge carriers in the material's space-charge layer, and is depicted as a spectrum in the complex coordinate plane (Fig. 12). At higher frequencies from 100 kHz to ∼1–3 kHz the spectral response is dominated by the RC time constant of the cell (i.e., the double layer/Helmholtz capacitance and charge transfer resistance), as discussed by *Ponomarev* and *Peter* in their seminal work on IMPS,[63] and is similar for both films. The H' axis is sometimes called surface transfer efficiency, as it represents the proportion of photogenerated holes to transferred holes.[64] The low-frequency intercept is then a function of transfer (k_{ct}) and recombination (k_{rec}) rate constants (Eq. 5).

$$H'_{\omega\to 0} = \frac{k_{ct}}{k_{ct} + k_{rec}} \quad [5]$$

The unique feature of IMPS spectra is the semicircle which may appear at low frequencies (typically < 100 Hz) in the IVth quadrant of the coordinate plane. This is called the recombination semicircle and is indicative of surface recombination of photogenerated holes. The frequency at the apex of this semicircle is related to the sum of transfer and recombination rate constants (Eq. 6).

$$\omega_{LF} = k_{ct} + k_{rec} \quad [6]$$

Then some observations can be made from the spectra that had been obtained for a 200V-TiO_2/Cu_xO film (Fig. 11). The emergence of a recombination semicircle suggests that in 1 M KOH surface electron-hole recombination does occur at 0.6 V. The addition of CH_3OH improves the transfer efficiency (larger $H'_{\omega\to 0}$ value), because it is thermodynamically more favorable for the photogenerated holes to oxidize methanol rather than water. Recombination is also suppressed in the presence of methanol, which can be inferred from the smaller magnitude of the recombination semicircle. However, for more detailed analysis, rate constants should be considered.

In order to map the recombination properties of the heterostructured film, the characterization was expanded to include the effect of incident light intensity (I_0), and the applied potential was confined to 0.4 V–0.8 V. Additionally, IMPS spectra were obtained in the frequency range of 1 kHz–1 Hz, as this range includes most of the recombination data in this case. The obtained spectra are presented in Fig. S12. Here $H'_{\omega\to 0}$ values increase with applied potential and decrease with light intensity (because conversion efficiency is proportional to applied potential, and inversely proportional to I_0).

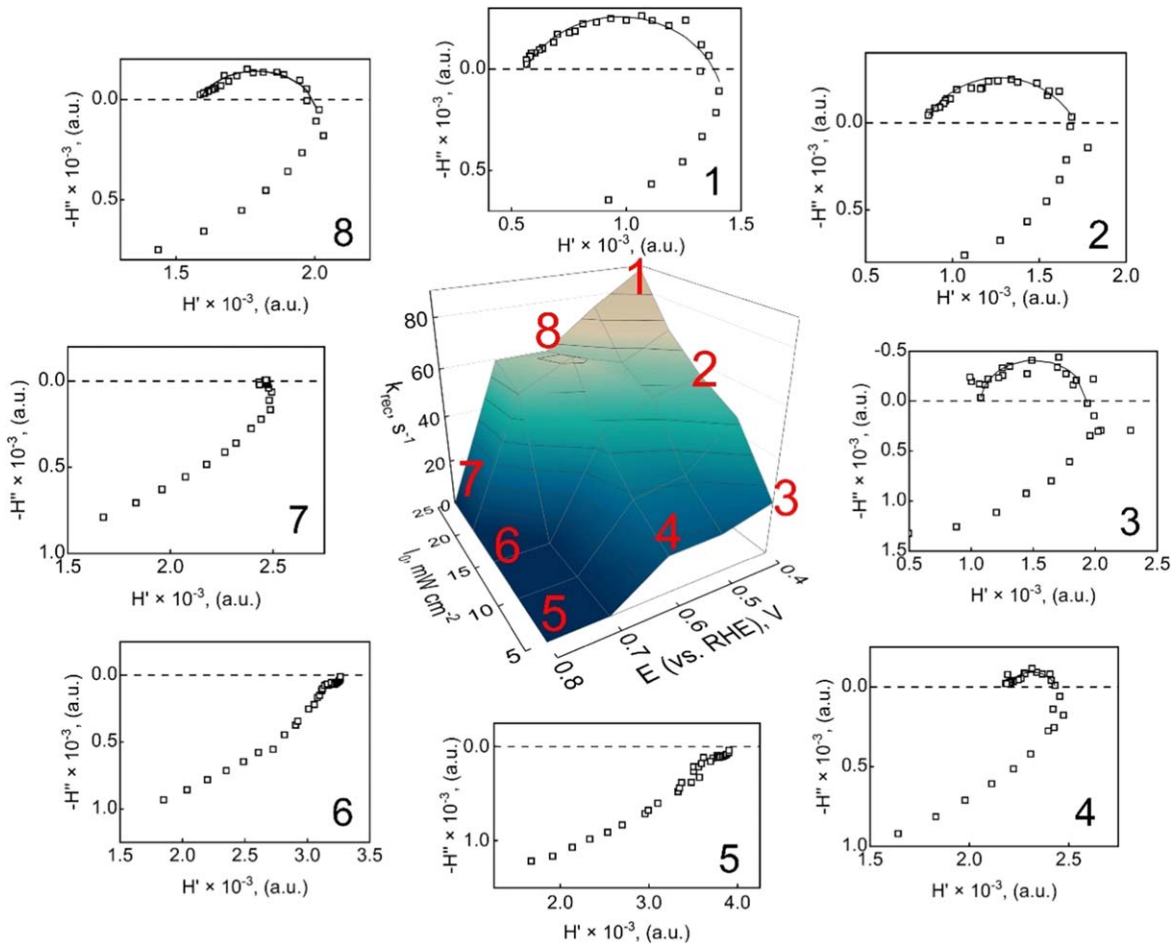

Figure 13. Recombination constant values and corresponding IMPS spectra at select E, I_0 values of 200V-TiO_2/Cu_xO film in 1 M KOH.

To obtain accurate ω_{LF} values, the recombination semicircle was mathematically fitted to the data points, and then the frequency corresponding to the apex of the semicircle was extracted. The k_{rec} values and select spectra are shown in Fig. 13 as a function of two variables—applied potential and light intensity. As expected, k_{rec} trends in the following ways: if I_0 is constant, k_{rec} decreases with increasing E, whereas if E is constant, k_{rec} decreases with decreasing I_0. Where no recombination semicircle could be discerned, k_{rec} was assumed to be 0. To generalize, broader semicircles typically correspond to larger ω_{LF} values, and thus higher recombination rate constants. The transfer constant (k_{ct}) is inversely related to k_{rec} (Eq. 6), so k_{ct} values are larger when k_{rec} values decrease. This mapping of low-overpotential photoanode hole recombination properties gives a comprehensive understanding of the photoelectrochemical performance of the system. It must be noted that, while electron-hole recombination is, in a sense, an intrinsic property of a photoanode, it can be mitigated by changing experimental conditions.

Lastly, an identical characterization was carried out in the electrolyte with 5% CH_3OH. The obtained IMPS spectra are shown in Fig. S13. Here a discernible recombination semicircle was formed only in three cases $-25\ mW\ cm^{-2}$ at 0.4 V and 0.6 V, and at $20\ mW\ cm^{-2}$ at 0.4 V, i.e. the three conditions with the largest k_{rec} values in 1 M KOH. This is, of course, a positive result, as it means that all photogenerated holes are transferred and photon conversion is maximized. Also, according to Eq. 6, if $k_{rec} = 0$, then $\omega_{LF} = k_{ct}$. In practice this results in the emergence of a part of a semicircle at medium to low frequencies in the first quadrant of the complex coordinate plane. In previous research by our team, these semicircles were fitted to obtain k_{ct} values when no recombination exists,[58] but such analysis is not widespread in IMPS studies.

Conclusions

In this study TiO_2/Cu_xO heterostructures were successfully synthesized by PEO. The synthesis parameters (duration, maximum voltage E_{max}, solution composition) were shown to have a significant impact of the structural, morphological, and photoelectrochemical properties of the films. Thicker films with larger diameter pores were formed when the synthesis was allowed to proceed until a higher E_{max}. TiO_2/Cu_xO heterostructures had a stronger anatase TiO_2 signal in XRD, which could have been the effect of Na_3cit in the solution during synthesis. EDX analysis detected a larger amount of Cu (as well as S, P, Na) in the atomic composition of the films with increasing E_{max}, thus confirming that ions from the solution do incorporate into the film. Cu was found to exist in all possible oxidation states (0, +1, +2) by XPS, but cross-referencing the analysis with XANES strongly suggests the dominance of +2 at least in the 200V-TiO_2/Cu_xO sample. UV–vis spectroscopy revealed growing Cu^{2+}-related light absorption with increasing E_{max}, and the optical band gaps of all films fell within the 3.25 eV–3.35 eV range. All of the films were measured for their photoelectrochemical water splitting activity in 1 M KOH. It was found that overall, the heterostructures generated larger photocurrents, most likely due to a combination of their improved crystallinity and lower band gaps. Mott-Schottky analysis confirmed that the V_{fb} values of the TiO_2/Cu_xO films became more positive with increasing copper content, and the data was cross-referenced to Gartner-Butler plots

and observations from PEC measurements. The photoanode performance of all films was improved by the addition of methanol, which acted as a hole scavenger, and IMPS spectra revealed that this improvement could be at least partially related to the elimination of surface electron-hole recombination.

Acknowledgments

We acknowledge DESY (Hamburg, Germany), a member of the Helmholtz Association HGF, for the provision of experimental facilities. Parts of this research were carried out at PETRA III and we would like to thank Dr Edmund Welter for his assistance in using the P65 beamline. Beamtime was allocated for proposal I-20220930 EC.

This research has received funding from the Research Council of Lithuania (LMTLT), agreement No. S-PD-22–5 (TICAL).

ORCID

R. Levinas https://orcid.org/0000-0003-3324-6472
L. Tamasauskaite-Tamasiunaite https://orcid.org/0000-0001-7555-4399
E. Norkus https://orcid.org/0000-0003-4713-5650

References

1. A. Fujishima and K. Honda, *Nature*, **238**, 37 (1972).
2. X. Chen, S. Shen, L. Guo, and S. S. Mao, *Chem. Rev.*, **110**, 6503 (2010).
3. B. Wang, S. Shen, and S. S. Mao, *J. Materiomics*, **3**, 96 (2017).
4. K. Nakata and A. Fujishima, *J. Photochem. Photobiol. C Photochem. Rev.*, **13**, 169 (2012).
5. Q. Guo, C. Zhou, Z. Ma, and X. Yang, *Adv. Mater.*, **31**, 1901997 (2019).
6. X. Li, Y. Chen, Y. Tao, L. Shen, Z. Xu, Z. Bian, and H. Li, *Chem Catal.*, **2**, 1315 (2022).
7. M. Ni, M. K. H. Leung, D. Y. C. Leung, and K. Sumathy, *Renew. Sustain. Energy Rev.*, **11**, 401 (2007).
8. S. B. Patil, P. S. Basavarajappa, N. Ganganagappa, M. S. Jyothi, A. V. Raghu, and K. R. Reddy, *Int. J. Hydrog. Energy*, **44**, 13022 (2019).
9. B. Bakbolat, C. Daulbayev, F. Sultanov, R. Beissenov, A. Umirzakov, A. Mereke, A. Bekbaev, and I. Chuprakov, *Nanomaterials*, **10**, 1790 (2020).
10. D. Chen et al., *J. Clean. Prod.*, **268**, 121725 (2020).
11. Parul, K. Kaur, R. Badru, P. P. Singh, and S. Kaushal, *J. Environ. Chem. Eng.*, **8**, 103666 (2020).
12. C. K. Nuo Peh, X.-Q. Wang, and G. W. Ho, *Procedia Eng.*, **215**, 171 (2017).
13. M. Shaban, A. M. Ahmed, N. Shehata, M. A. Betiha, and A. M. Rabie, *J. Colloid Interface Sci.*, **555**, 31 (2019).
14. A. Sinhmar, H. Setia, V. Kumar, A. Sobti, and A. P. Toor, *Environ. Technol. Innov.*, **18**, 100658 (2020).
15. H. M. Mousa, J. F. Alenezi, I. M. A. Mohamed, A. S. Yasin, A.-F. M. Hashem, and A. Abdal-hay, *J. Alloys Compd.*, **886**, 161169 (2021).
16. L. Gnanasekaran, R. Pachaiappan, P. S. Kumar, T. K. A. Hoang, S. Rajendran, D. Durgalakshmi, M. Soto-Moscoso, L. Cornejo-Ponce, and F. Gracia, *Environ. Pollut.*, **287**, 117304 (2021).
17. D. Chauhan, V. R. Satsangi, S. Dass, and R. Shrivastav, *Bull. Mater. Sci.*, **29**, 709 (2006).
18. Q. Shi, G. Ping, X. Wang, H. Xu, J. Li, J. Cui, H. Abroshan, H. Ding, and G. Li, *J. Mater. Chem. A*, **7**, 2253 (2019).
19. M. Khalil, E. S. Anggraeni, T. A. Ivandini, and E. Budianto, *Appl. Surf. Sci.*, **487**, 1376 (2019).
20. J. Singh, K. Sahu, B. Satpati, J. Shah, R. K. Kotnala, and S. Mohapatra, *J. Phys. Chem. Solids*, **135**, 109100 (2019).
21. L. Barrientos, P. Allende, M. Á. Laguna-Bercero, J. Pastrián, J. Rodriguez-Becerra, and L. Cáceres-Jensen, *J. Phys. Chem. Solids*, **119**, 147 (2018).
22. M. M. Ahmad, S. Mushtaq, H. S. Al Qahtani, A. Sedky, and M. W. Alam, *Crystals*, **11**, 1456 (2021).
23. A. M. Alotaibi, S. Sathasivam, B. A. D. Williamson, A. Kafizas, C. Sotelo-Vazquez, A. Taylor, D. O. Scanlon, and I. P. Parkin, *Chem. Mater.*, **30**, 1353 (2018).
24. C. D. Lokhande, S.-K. Min, K.-D. Jung, and O.-S. Joo, *J. Mater. Sci.*, **40**, 491 (2005).
25. K. Indira, U. K. Mudali, T. Nishimura, and N. Rajendran, *J. Bio- Tribo-Corros.*, **1**, 28 (2015).
26. P. Rivera Bermudez, V. Alarcón Rodríguez, and G. Peña-Rodríguez, *J. Phys. Conf. Ser.*, **2046**, 012041 (2021).
27. V. Sivaprakash and R. Narayanan, *Mater. Today Proc.*, **37**, 142 (2021).
28. P. Roy, S. Berger, and P. Schmuki, *Angew. Chem. Int. Ed.*, **50**, 2904 (2011).
29. M. Aliofkhazraei et al., *Appl. Surf. Sci. Adv.*, **5**, 100121 (2021).
30. X. Zhang, G. Cai, Y. Lv, Y. Wu, and Z. Dong, *Surf. Coat. Technol.*, **400**, 126202 (2020).
31. A. R. Ribeiro et al., *Mater. Sci. Eng. C*, **54**, 196 (2015).
32. R. Levinas, N. Tsyntsaru, H. Cesiulis, R. Viter, K. Grundsteins, L. Tamašauskaitė-Tamašiūnaitė, and E. Norkus, *Coatings*, **13**, 673 (2023).
33. E. Welter, R. Chernikov, M. Herrmann, and R. Nemausat, *AIP Conf. Proc.*, **2054**, 040002 (2019).
34. A. Kalinko, (2023), XAESA v.0.07 (https://gitlab.desy.de/aleksandr.kalinko/xaesa).
35. A. Kuzmin and J. Chaboy, *IUCrJ*, **1**, 571 (2014).
36. G. Mortazavi, J. Jiang, and E. I. Meletis, *Appl. Surf. Sci.*, **488**, 370 (2019).
37. X. Wei, G. Zhu, J. Fang, and J. Chen, *Int. J. Photoenergy*, **2013**, 1 (2013).
38. H. Ijadpanah-Saravy, M. Safari, A. Khodadadi-Darban, and A. Rezaei, *Anal. Lett.*, **47**, 1772 (2014).
39. M. Kaseem and B. Dikici, *Coatings*, **11**, 374 (2021).
40. Z. H. Gan, G. Q. Yu, B. K. Tay, C. M. Tan, Z. W. Zhao, and Y. Q. Fu, *J. Phys. Appl. Phys.*, **37**, 81 (2004).
41. J. Ghijsen, L. H. Tjeng, J. Van Elp, H. Eskes, J. Westerink, G. A. Sawatzky, and M. T. Czyzyk, *Phys. Rev. B*, **38**, 11322 (1988).
42. "NIST X-ray Photoelectron Spectroscopy Database." *NIST Standard Reference Database Number 20*, .
43. C. Fan, C. Chen, J. Wang, X. Fu, Z. Ren, G. Qian, and Z. Wang, *Sci. Rep.*, **5**, 11712 (2015).
44. E. McCafferty and J. P. Wightman, *Surf. Interface Anal.*, **26**, 549 (1998).
45. L. Xu, Y. Yang, Z.-W. Hu, and S.-H. Yu, *ACS Nano*, **10**, 3823 (2016).
46. A. J. Veinot, A. Al-Rashed, J. D. Padmos, I. Singh, D. S. Lee, M. R. Narouz, P. A. Lummis, C. J. Baddeley, C. M. Crudden, and J. H. Horton, *Chem.—Eur. J.*, **26**, 11431 (2020).
47. M. C. Biesinger, *Surf. Interface Anal.*, **49**, 1325 (2017).
48. T. Yano, M. Ebizuka, S. Shibata, and M. Yamane, *J. Electron. Spectrosc. Relat. Phenom.*, **131–132**, 133 (2003).
49. A. Gaur, B. D. Shrivastava, and S. K. Joshi, *J. Phys. Conf. Ser.*, **190**, 012084 (2009).
50. S. Chandarak, J. Jutimoosik, S. Pojprapai, S. Srilomsak, S. Rujirawat, R. Yimnirun, and T. Monnor, *Ferroelectrics*, **422**, 23 (2011).
51. Z. Chen et al., *Photoelectrochemical Water Splitting, SpringerBriefs in Energy.* (New York, NY)(Springer New York)p. 49 (2013).
52. B. Choudhury, M. Dey, and A. Choudhury, *Appl. Nanosci.*, **4**, 499 (2014).
53. A. Kapoor, Pratibha, and J. K. Rajput, *J. Mol. Liq.*, **366**, 120280 (2022).
54. A. S. Ethiraj and D. J. Kang, *Nanoscale Res. Lett.*, **7**, 70 (2012).
55. D. A. Bopape, S. Mathobela, N. Matinise, D. E. Motaung, and N. C. Hintsho-Mbita, *Catalysts*, **13**, 163 (2023).
56. S. Sundar, G. Venkatachalam, and S. Kwon, *Nanomaterials*, **8**, 823 (2018).
57. S. Bisht, M. Ghalwan, A. D. Oza, K. K. Saxena, and C. Prakash, *Int. J. Interact. Des. Manuf. IJIDeM* (2023).
58. R. Levinas, N. Tsyntsaru, T. Murauskas, and H. Cesiulis, *Front. Chem. Eng.*, **3**, 760700 (2021).
59. K. Sivula, *ACS Energy Lett.*, **6**, 2549 (2021).
60. A. Hankin, F. E. Bedoya-Lora, J. C. Alexander, A. Regoutz, and G. H. Kelsall, *J. Mater. Chem. A*, **7**, 26162 (2019).
61. F. Amano, *Solar-to-Chemical Conversion*, ed. H. Sun (New York)(Wiley)p. 163 (2021).
62. F. Amano, M. Tian, B. Ohtani, and A. Chen, *J. Solid State Electrochem.*, **16**, 1965 (2012).
63. E. A. Ponomarev and L. M. Peter, *J. Electroanal. Chem.*, **396**, 219 (1995).
64. S. Ravishankar, A. Riquelme, S. K. Sarkar, M. Garcia-Batlle, G. Garcia-Belmonte, and J. Bisquert, *J. Phys. Chem. C*, **123**, 24995 (2019).